

NRC Publications Archive Archives des publications du CNRC

Insights into the effect of various supports on hydrothermal liquefaction of food waste over iron-oxide nano-catalysts

Ebrahim, Sayed Ahmed; Jiang, Xin; Kodra, Oltion; Couillard, Martin;
Baranova, Elena; Singh, Devinder

For the publisher's version, please access the DOI link below./ Pour consulter la version de l'éditeur, utilisez le lien DOI ci-dessous.

<https://doi.org/10.2139/ssrn.4690567>

NRC Publications Archive Record / Notice des Archives des publications du CNRC :

<https://nrc-publications.canada.ca/eng/view/object/?id=533eb5a8-ebc1-4876-ba87-3717f26d9142>

<https://publications-cnrc.canada.ca/fra/voir/objet/?id=533eb5a8-ebc1-4876-ba87-3717f26d9142>

Access and use of this website and the material on it are subject to the Terms and Conditions set forth at

<https://nrc-publications.canada.ca/eng/copyright>

READ THESE TERMS AND CONDITIONS CAREFULLY BEFORE USING THIS WEBSITE.

L'accès à ce site Web et l'utilisation de son contenu sont assujettis aux conditions présentées dans le site

<https://publications-cnrc.canada.ca/fra/droits>

LISEZ CES CONDITIONS ATTENTIVEMENT AVANT D'UTILISER CE SITE WEB.

Questions? Contact the NRC Publications Archive team at

PublicationsArchive-ArchivesPublications@nrc-cnrc.gc.ca. If you wish to email the authors directly, please see the first page of the publication for their contact information.

Vous avez des questions? Nous pouvons vous aider. Pour communiquer directement avec un auteur, consultez la première page de la revue dans laquelle son article a été publié afin de trouver ses coordonnées. Si vous n'arrivez pas à les repérer, communiquez avec nous à PublicationsArchive-ArchivesPublications@nrc-cnrc.gc.ca.

Insights into the effect of various supports on hydrothermal liquefaction of food waste over iron-oxide nano-catalysts

Sayed Ahmed Ebrahim^{a,b}, Xin Jiang^b, Oltion Kodra^b, Martin Couillard^b, Elena A. Barancova^a, Devinder Singh^{b*}

^a Department of Chemical and Biological Engineering, Centre for Catalysis Research and Innovation (CCRI), Nexus for Quantum Technologies (NexQT), University of Ottawa, Ottawa, Ontario, K1N 6N5, Canada

^b Energy, Mining, and Environment Research Centre, National Research Council of Canada, Ottawa ON, K1A 0R6, Canada

*Corresponding author: Devinder.Singh@nrc-cnrc.gc.ca, Tel: 613-991-5033

Abstract

This work investigates the effect of supported iron-oxide nano-catalysts for hydrothermal conversion of food waste. The studied supports were carbon black (Vulcan carbon), reducible oxide (CeO₂), ZSM-5 and amorphous SiO₂-Al₂O₃. Catalytic hydrothermal liquefaction experiments were carried in a batch reactor at 21 MPa and 300 °C. Different fractions of Fe(0), Fe²⁺ and Fe³⁺ alters its tendency toward deoxygenation, hydrogenations and condensation reactions, which influence the bio-crude yield, elemental compositions, and energy recoveries. The fresh and spent catalysts were characterized using X-ray photoelectron spectroscopy, physisorption analysis, thermogravimetric analysis, transmission and scanning electron microscopy. It was found that the change in support has different promotional effects in favouring certain HTL pathways and products. Catalysts with high fractions of Fe²⁺ relative to Fe³⁺ increased the yield of oil-soluble products and overall energy recovery, while the presence of Fe(0) sites reduced the oxygen content and improved the bio-crude heating values.

Keywords:

Hydrothermal liquefaction, Iron-oxide catalyst, Food waste, Bio-crude, Asphaltenes

1 Introduction

Fossil fuels have served humanity as a reliable, cost-efficient, and easily transportable source of energy. However, GHG emissions associated with its use have led to severe environmental concerns endangering the sustainability of life on earth. Advanced biofuels are expected to play a significant role in furthering GHG reduction targets [1]. Waste feedstocks (agricultural, household, and industrial) offer cheap and sustainable starting material for these processes [2]. The average loss of food to waste is estimated between 124-154 kg per capita per year. Considering the rise in the global population, this rate would logically keep increasing unless appropriate actions are undertaken[3]. A significant portion of this ends up in landfills. Organic waste including food waste can be utilized to potentially replace fossil fuel while alleviating the waste management challenge [4].

Food waste valorisation into bio-oil through thermochemical routes such as pyrolysis and hydrothermal liquefaction (HTL) has revealed promising results. However, further progress is required to improve the economics (mainly influenced by oil yield and its quality [5]) and upgrading aspects before commercialisation. The HTL process can accept a wide range of wet feedstocks [6], [7]. The process is operated at a lower temperature and higher pressure than pyrolysis, and typically produces bio-crude with higher heating values due to the higher carbon and a lower heteroatom content. Additional upgrading steps are usually required before being used as transportation fuel [8]. Catalysts can be employed to improve the sustainability and economics of HTL process by increasing the oil conversion yield and/or improving the bio-crude quality [9].

Heterogeneous catalysts are preferred for their ease of recyclability, although, challenges like coking, poisoning, etc need to be overcome before commercial applications [10]. Iron as an abundant, cheap and moderately nontoxic metal has been attractive in the catalysis industry. Its multiple oxidation states makes it effective in a wide range of organic reactions [11] [12] [13], [14], [15].

In recent years, the interest has been increasing toward studying iron-based heterogeneous catalysts in hydrothermal liquefaction of various biomass materials such as algae [16], food processing wastes [17], and lignocellulosic materials [18]. Zero valent Fe for HTL of oak wood increased bio-crude yields by 17 wt%. The HHV's of biocrude also increased due to the enhanced hydrogenation and deoxygenation reactions [18]. Iron at different oxidation states has also been investigated for Oak wood at 300 °C [19]. Fe₂O₃ produced 3 wt% higher char yield than Fe₃O₄ and 5 wt% higher than Fe. The biocrude yield increased by 6wt%, 1wt% and 10 wt% using Fe₃O₄, Fe₂O₃ and Fe respectively [19]. Red mud as a natural catalyst containing around 45% Fe₂O₃ was used in HTL of *Spirulina* at 300 °C before and after activation. Unactivated red mud (surface area; 14 m²g⁻¹) and activated red mud (surface area: 188 m²g⁻¹) increased the bio-crude yield by 8 and 13 wt%, respectively. The increase in bio-crude yields was also associated with oxygen increase by 2.5-5% and HHV's reduction by up to 1.3 MJ kg⁻¹ [20]. Nanocrystalline Fe₃O₄ was studied for HTL of *Ulva-fasciata* at 300 °C. Increasing the catalyst loading from 0.63 to 3.75 wt% caused a reduction in bio-crude yield by 8 wt% and oxygen production by 4.5 wt% accompanied by an increase in the char formation [21]. Fe/TiO₂ was tested for *Nannocloropsis* at 300 °C, and showed no impact on biocrude yield and HHV [22]. Unsupported iron-oxide on ZSM-5 was tested for soy protein and sunflower oil at 350 °C, a reduction in bio-crude yield by 2-30 wt% and decrease in HHV's by 0.5-0.8 MJ kg⁻¹ was noted for both feedstocks [23].

The above-mentioned studies suggest that iron in different forms and supported on various supports may influence the HTL process differently. There are no studies in the literature that systematically investigate the effect of iron supported on different supports. Furthermore, the catalyst deactivation issues for HTL of wastes have not received a significant attention. This study aims to develop an understanding of the synergetic effect of iron-oxides catalysts with its supports, and possible catalyst deactivation sources. This is done by testing iron on four different supports (Vulcan carbon, CeO₂, SiO₂-Al₂O₃ and ZSM-5) having diverse characteristics and textural properties with possible sources of deactivation studied by characterisation of catalyst after repeated use. The influence of catalysts is evaluated by comparing the changes in bio-crudes energy recoveries (combined factor of yields and HHV's), boiling points fractions, relative compositions of various functional groups and tendency of each support to produce asphaltenes through polycondensation.

2 Experimental

2.1 Materials

The feedstock used in this study consists of equal proportions (dry basis) of mixed vegetable and white meat which represent two of the main constituents in domestic food wastes [24]–[26]. The feedstock constituents were blended and water content adjusted to 85 wt% using distilled water. See **Table 1** for proximate and ultimate analysis of the feedstock used in this study. Similar feedstocks have been used in other studies [27], [28]. The catalysts were synthesized using Iron (III) nitrate nonahydrate ($\geq 98\%$) purchased from Sigma Aldrich, ethylene glycol (99.5%) and tetramethylammonium hydroxide pentahydrate (98%) purchased from Thermo Fischer Scientific, and ammonium molybdate tetrahydrate (99%) purchased from Alfa Aesar. The catalyst supports were Cerium (IV) oxide nanopowder (99.5%) from Alfa Aesar, Vulcan XC-72 from Cabot, Silica-alumina grade 13 from Sigma Aldrich and ZSM-5 (CBV3004E) from Zeolyst. The solvents used for bio-crude and asphaltenes extractions were methylene chloride ($\geq 99.5\%$), n-pentane ($\geq 99\%$) and toluene ($\geq 99.9\%$) purchased from Fischer Chemical. Residual oil and sulfanilamide used as standards for elemental analysis were purchased from DECO corporation. Deuterated chloroform (99.8 atom%) used for NMR samples was purchased from ACP Chemicals. Hydrochloric acid (34-37%) and nitric acid (67-70 wt%) used in catalysts digestion was purchased from Aristar Plus. Standard elements used for ICP-OES were obtained from PlasmaCAL.

Table 1

Proximate, ultimate analysis and biochemical compositions of food waste. (Replicates with $n \geq 3$ represented as mean \pm standard deviation).

Properties	Value
Proximate Analysis	(wt. %)
Moisture	85.4 \pm 2.7
Ash	2.1 \pm 0.3
Ultimate Analysis	
C (%)	52.36 \pm 0.05
H (%)	7.01 \pm 0.28
O (%)	33.62 \pm 0.41
N (%)	6.38 \pm 0.10
S (%)	0.6 \pm 0.07

HHV (MJ/kg)	23.63
Biochemical Composition	
Carbohydrate	49.5
Protein	32.5
Lipid	15.4

2.2 Procedure

2.2.1 Catalyst synthesis

Iron-oxide colloidal was synthesized following the polyol synthesis as detailed in a previous study [29]. Iron-oxide precursor, iron nitrate nonahydrate ($\text{Fe}(\text{NO}_3)_3 \cdot 9\text{H}_2\text{O}$) was mixed with ethylene glycol (EG) that acts as a solvent and a reducing agent. An alkaline reagent solution of 0.25 M tetramethylammonium hydroxide (TMAOH) in EG was added to the iron precursor solution in droplets until the pH was 12. The final solution was refluxed until the temperature reached 160 °C and then cooled to room temperature. Molybdenum oxide colloidal was also synthesized using polyol synthesis method. Molybdenum oxide precursor, ammonium molybdate tetrahydrate ($(\text{NH}_4)_6\text{Mo}_7\text{O}_{24} \cdot 4\text{H}_2\text{O}$) was mixed with EG. The pH of the solution was adjusted to 10 by adding drops of 0.25 M TMAOH in EG. The solution was then refluxed at 160 °C for 75 minutes. The supported catalysts were prepared following the wet impregnation method by dissolving the catalyst supports in DI water before adding drops of iron-oxide and molybdenum oxide colloidal. All fresh catalysts were subjected to 5% H_2/Ar at 250 °C for 5 h before HTL experiments.

2.2.2 HTL experiment

The experiment was carried in a 250 mL batch autoclave. The reactor containing 130 g of food waste and 1.95 g (10 wt% based on dry mass) of catalyst was purged with argon and pressurized with 50% H_2/Ar to a total initial pressure of 4 MPa. The process temperature was controlled at 300 °C for 60 min (final pressure around 16 MPa) before cooling to room temperature (refer to the supporting information for the heating and cooling curves). The product inside the reactor was mixed with methylene chloride and stirred for 5 min, followed by filtration using 0.45 μm PTFE filter. The oil phase was separated from the aqueous phase using a separatory funnel. Methylene chloride solvent was separated from bio-crude using rotary evaporation for 25 min at conditions

of 25 °C at 400 kPa, followed by 20 min at 32 °C at 15 kPa. The yields are calculated using Eq. (1-3) (data presented as mean ± standard deviation, n≥3)

Asphaltenes were extracted from bio-crudes using the procedure described elsewhere [27]. Asphaltene yield was calculated using Eq. (4).

$$Y_{bio-crude} (\%) = \frac{m_{bio-crude}(g)}{m_{FW}(g) - m_{moisture}(g) - m_{ash}(g)} * 100 \quad (1)$$

$$Y_{solid} (\%) = \frac{m_{oxidizable\ solids}(g)}{m_{FW}(g) - m_{moisture\ in\ FW}(g) - m_{ash\ in\ FW}(g)} * 100 \quad (2)$$

$$Y_{gas+aqueous} (\%) = 100 - Biocrude\ yield (\%) - Char\ yield (\%) \quad (3)$$

$$Y_{Asphaltenes} (\%) = \frac{m_{asphaltenes}(g)}{m_{bio-crude}(g)} * 100 \quad (4)$$

2.2.3 Catalyst characterization

The textural properties of catalysts were determined by nitrogen physisorption using ASAP 2020 Micrometrics after degassing the samples at 250 °C for 3 h under vacuum. The adsorption-desorption data was acquired at 77 K. Catalyst metal loading was determined using inductively coupled plasma-optical emission spectrometry (ICP-OES): Perkin Elmer Optima 3000 after acid digestion. Scanning electron microscopy (SEM) was performed using Hitachi SU5000 FE-SEM. EDS maps were acquired with Oxford EDS detector and processed using Aztec software. A FEI Titan3 80–300 TEM operated at 300 keV, and equipped with a CEOS aberration corrector for the probe forming lens and a monochromated field-emission gun was used to acquire both high-resolution TEM (HRTEM) and annular dark-field (ADF) images. TEM specimens were prepared by dispersing the solid powder in ethanol, and sonicating for 15 min. One drop of the solution was then placed onto a 200 mesh TEM copper grid coated with a lacey carbon support film (Ted Pella) and dried in air. The holes in the lacey films allow for the acquisition of spectroscopy signals without interference signals from the carbon support. ADF images were collected using a high-angle annular dark-field (HAADF) Fischione detector in scanning transmission electron microscopy (STEM) mode. This technique provides signal intensity related mainly to the atomic number (Z) and the thickness of the region analyzed. The TEM instrument is also equipped

with an energy-dispersive X-ray (EDX) spectrometer (EDAX Analyzer, DPP-II). To optimize the signal intensity, EDX spectra were acquired with the specimen tilted at 15 degrees.

The surface chemistry of fresh and spent catalysts was characterised by X-ray photoelectron spectroscopy (XPS) using Kratos Axis Ultra DLD with a monochromatic Al K α as X-ray source (140 W). Survey scans were obtained at a pass energy of 80 eV and high-resolution analysis was obtained at 20 eV. Kratos charge neutralizer was used, and the analysis was carried in a vacuum of 5×10^{-9} torr. XPS spectra were fitted using CasaXPS software to get the best fitted curves at minimal root mean square after calibrating the binding energy to the adventitious carbon 284.8 eV. High resolution XPS of spent FeO $_x$ /CeO $_2$ resulted in noisy and indistinguishable peaks and was not included in the manuscript. Coke disposition on catalyst was determined by the weight difference after combusting the solids recovered from HTL under air at 850 °C. To determine the mass of carbon deposition on catalysts, 5 mg of spent catalysts were subjected to TGA programmed to reach a temperature of 850 °C at a ramp rate of 10 °C/min. The weight of deposited carbon in VC supported catalysts was estimated by considering the weight loss for the fresh and the spent catalysts.

2.2.4 Bio-crude and asphaltenes characterization

The elemental analysis of bio-crude was determined using Vario EL cube Analyzer. Residual oil and sulfanilamide standards were used for calibration. The oxygen content was determined by difference. The HHV's were calculated using Boie's equation (Eq. (5)), and the energy recovery was calculated using Eq. (6). Thermogravimetric analysis (TGA) was performed using TA Instruments model Q5000 IR. The sample was heated to 700 °C at a ramp rate of 50 °C min $^{-1}$ under nitrogen flowrate of 25 mL min $^{-1}$. Gas chromatography-mass spectroscopy (GC-MS) was used as a semi-quantitative technique to identify the components using Agilent 5975c GC equipped with DB-5MS column (30 m length, 0.25 mm ID and 0.25 thickness). The samples were injected at a split ratio of 1:5, and the generated peaks were identified using NIST library. Proton nuclear magnetic resonance (^1H NMR) was conducted using Bruker AVANCE 300 with a resonance frequency of 300 MHz. The samples were mixed with CDCl $_3$, and the spectra was acquired at 32 scan and 90° pulse. The Fourier transform infrared (FTIR) spectra was acquired using Nicolet 6700 equipped with diamond ATR accessory. The spectra was obtained in the range 4000-525 cm $^{-1}$ at a resolution of 4 cm $^{-1}$.

$$HHV (MJ/kg) = 35.16 C + 116.225H - 10.09O + 6.28 N + 10.465S \quad (5)$$

$$ER (\%) = \frac{HHV_{bio-crude}}{HHV_{FW}} * Y_{bio-crude} (\%)$$

3 Results and Discussion

3.1 Catalyst characterization

The characteristics of catalysts supports such as surface area and porosity influence its activity by offering a reasonable contact surface area and appropriate pore sizes that allow access to active sites. Nitrogen adsorption isotherms were carried out to analyze the physisorption characteristics of catalysts and are presented in **Fig. 1**. In accordance with IUPAC classification, all catalysts show type IV isotherms with hysteresis loops typically of types H2 ($FeO_x/SiO_2-Al_2O_3$), H3 (FeO_x/VC) and H4 (FeO_x/CeO_2 and $FeO_x/ZSM-5$) with pore shapes mostly like ink-bottle shaped (H2) and slit-shaped pores (H3 and H4). The pore volume, pore size and BET surface area of catalysts are shown in **Table 2**. Pore size distribution of catalysts can be found in the supplementary material. The average pore diameter of all the catalysts are in the range of mesoporous materials. Catalysts with $SiO_2-Al_2O_3$ supports had the highest surface area and distinguishably high pore volumes in comparison with other supports. The decrease in pore sizes can be beneficial for increasing the surface area but can also make it susceptible to pore blockage during processing of biochemical compounds[30].

The chemical states of iron-oxide supported catalysts were investigated before and after HTL using XPS analysis. The main Fe 2p peaks of fresh catalysts correspond to Fe^{2+} (FeO) and Fe^{3+} (Fe_2O_3) at different ratios (**Fig. 2** and **Table 3**). The orbitals of Fe $2p_{3/2}$ were fitted with Fe^{2+} and Fe^{3+} with binding energies near 710 eV and 712 eV, respectively. The orbitals of Fe $2p_{1/2}$ were fitted with Fe^{2+} and Fe^{3+} with binding energies near 723 eV and 726 eV [31]. The peaks shift to higher or lower binding energies depending on the strength of interactions between iron sites and the supports. Iron orbitals appeared at lower binding energies in fresh FeO_x/CeO_2 catalyst which imply a strong interaction between CeO_2 and iron-oxide nanoparticles. XPS peaks of Fe(0) was also noted in FeO_x/CeO_2 which also indicate a reduction of iron on the support sites. The ratios between relative fractions of Fe^{3+} and Fe^{2+} varied depending on the support. The fitted peaks for Mo 3d in

the fresh FeO_x-MoO_x/VC correspond to Mo (0), Mo⁵⁺ and Mo⁶⁺ at binding energies near 228.1 eV, 231.5 eV and 232.7 eV [32]. The presence of a higher electronegative transition metal MoO_x sites seem to oxidize FeO_x sites, as noted with a high relative content of Fe³⁺ and the presence of Mo(0) sites in FeO_x-MoO_x/VC (**Fig. 2** and **Table 3**).

Iron-oxide supported catalysts show uniform distribution as shown in SEM-EDX mappings and TEM-EDX in **Fig. 3**.

Table 2
Textural properties of fresh catalysts

Material	Fe (wt%)	Mo (wt%)	S _{BET} (m ² /g)	Pore Volume (cm ³ /g)	Pore Size (nm)
CeO ₂	-	-	70.71	0.126	7.286
FeO _x /CeO ₂	4.74	-	47.63	0.082	7.710
VC	-	-	221.22	0.293	8.557
FeO _x /VC	5.44	-	73.75	0.154	8.114
FeO _x -MoO _x /VC	2.47	2.72	152.02	0.163	7.700
SiO ₂ -Al ₂ O ₃	-	-	418.88	0.553	4.836
FeO _x /SiO ₂ -Al ₂ O ₃	4.23	-	348.52	0.460	4.706
ZSM-5	-	-	335.01	0.107	3.703
FeO _x /ZSM-5	4.64	-	156.48	0.079	5.721

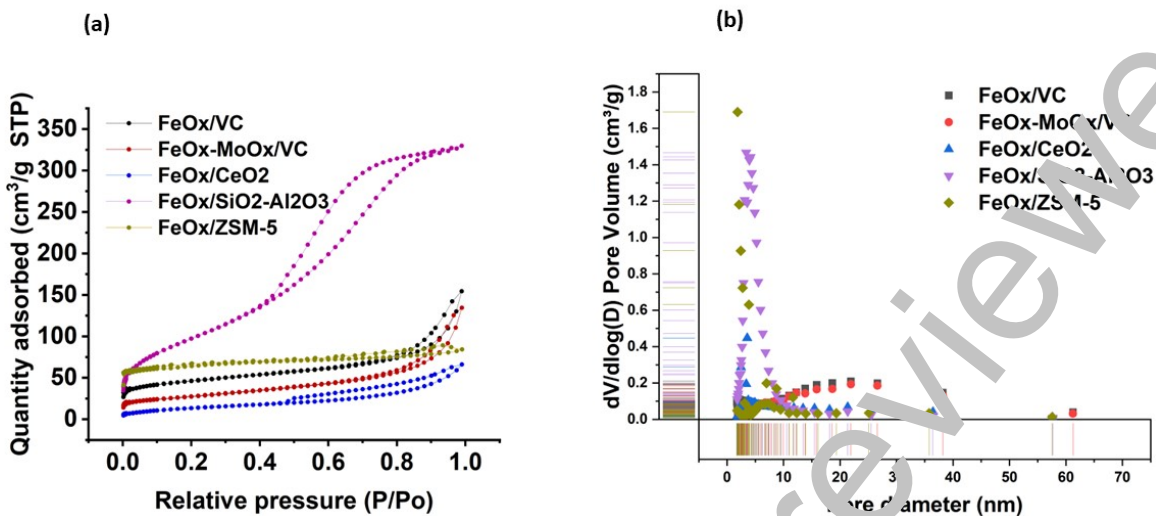


Fig. 1. nitrogen adsorption/desorption for iron-oxide supported catalysts

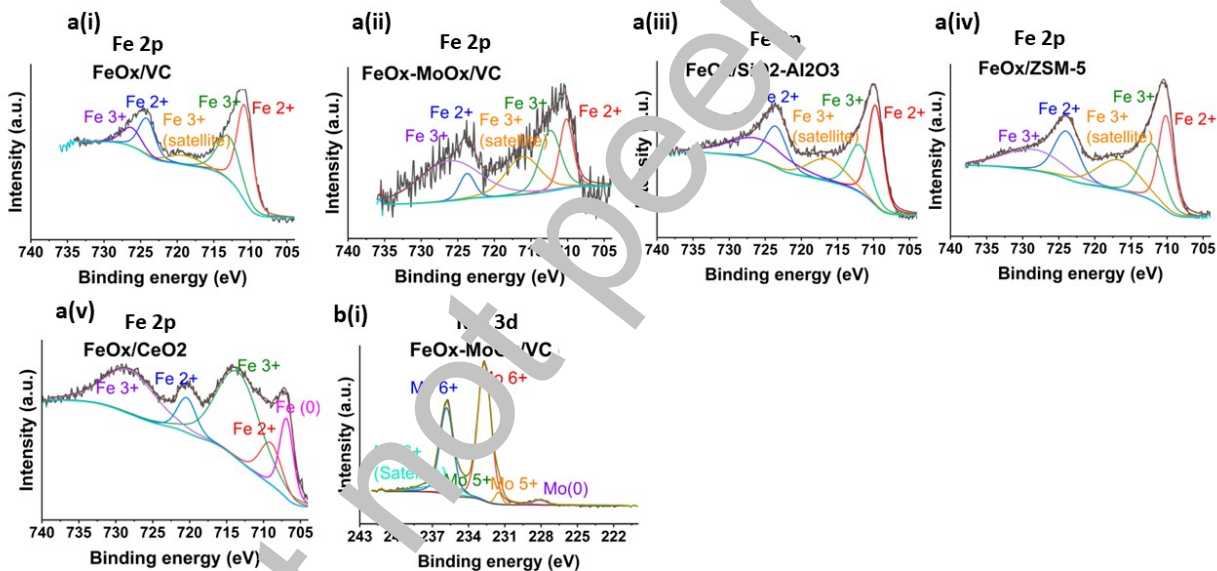


Fig. 2. XPS spectrum of a) Fe 2p and b) Mo 3d in fresh iron-supported catalysts

Table 3

XPS binding energies and fractions of Fe 2p and Mo 3d in fresh catalysts

	Fe(0)	Fe ²⁺	Fe ³⁺	Fe ³⁺ , satellite	Fe ³⁺ /Fe ²⁺ relative ratios
FeOx/VC	-	710.27	712.44	718.46	0.80

FeO _x -MoO _x /VC	-	710.17	712.37	716.11	18.49	
FeO _x /SiO ₂ -Al ₂ O ₃	-	710.24	712.43	716.17	1.33	
FeO _x /ZSM-5	-	710.14	712.11	716.57	1.57	
FeO _x /CeO ₂	707.08	709.23	713.59	-	2.00	
	Mo (0)	Mo ⁵⁺	Mo ⁶⁺	Mo ⁵⁺	Mo ⁶⁺	Mo ⁶⁺ satellite
FeO _x -MoO _x /VC	228.12	231.52	232.69	234.77	235.82	236.82

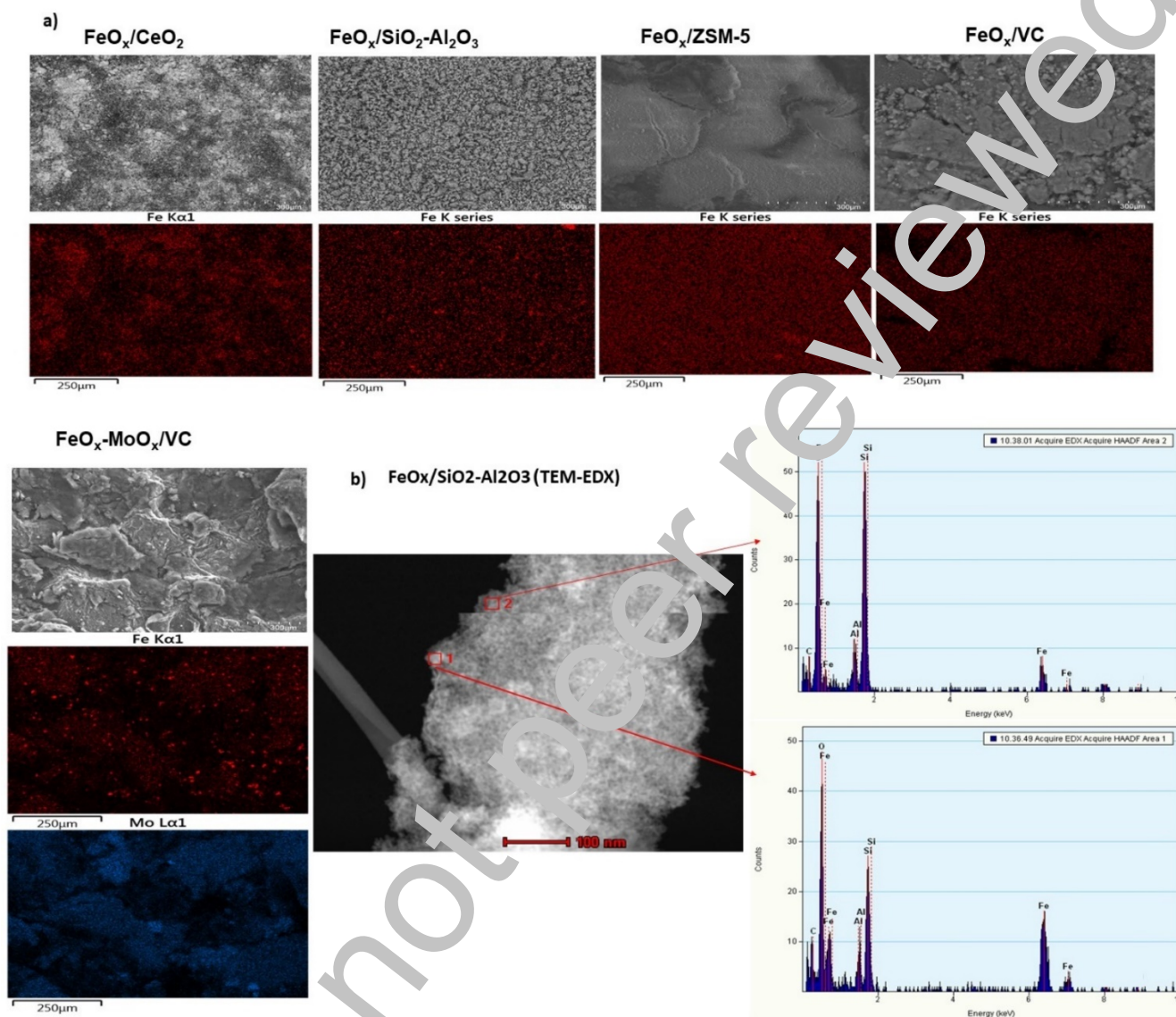


Fig. 3. distribution of elements in fresh iron-oxide supported catalysts using a) SEM-EDX mapping and b) TEM-EDX

3.2 Effect of supported iron-oxide catalysts on bio-crude yields

The effect of iron-oxide catalysts was determined by comparing the influence of the supports on the yield before and after adding iron-oxide. Four different supports with various features were covered in this study: Vulcan carbon (VC), CeO_2 , ZSM-5 and $\text{SiO}_2\text{-Al}_2\text{O}_3$. The results in **Fig. 4** show that iron-oxide may increase or decrease the biocrude yield depending on the type of support and iron sites. Most iron-oxide catalysts promoted the formation of oil soluble compounds (62-65

wt%) and reduced the char formation when compared to their respective supports. Iron-oxide supported by CeO_2 showed a decrease in bio-crude yield to 50 wt% accompanied by an increase

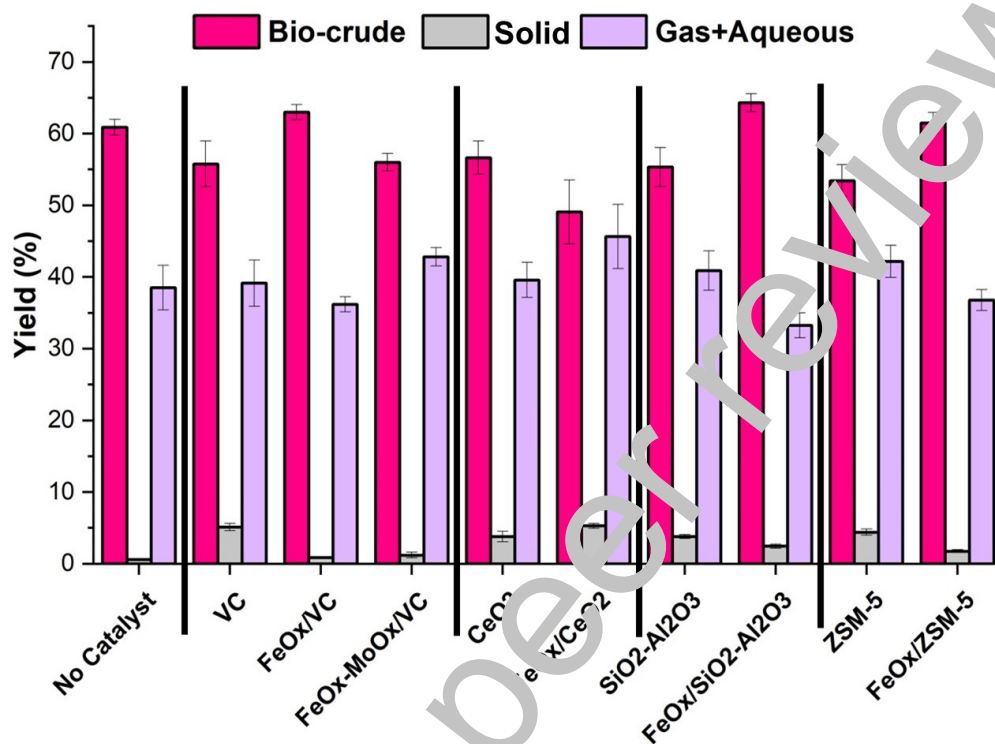


Fig. 4. Bio-crude, oxidizable solids, aqueous and gas yields produced from HTL of food waste at 300 °C, 21 MPa and 1h. (Replicates with $n \geq 3$ and error represented as standard deviation).

in gaseous and aqueous fractions to 46 wt%. The decrease in the bio-crude yield using $\text{FeO}_x/\text{CeO}_2$ is attributed to the presence of Fe (0) sites on its surface (**Fig. 2**), which could have promoted deoxygenation and degradation reactions and decreased quantity of oil-soluble compounds. This is also evidenced by much lower oxygen content of bio-crude (see Table 4). Iron-oxide supported on VC showed increased bio-crude yield (63 wt%) compared to 56 wt % for VC, and significant reduction in char from 5wt% using VC to 0.9 wt% using FeO_x/VC . The increase in the bio-crude yield in iron-oxide supported catalysts was also associated with the presence of high fractions of Fe^{2+} relative to Fe^{3+} on the catalyst surface (**Table 3**).

3.2 Elemental analysis of bio-crude

The influence of different iron-oxide catalysts on the bio-crude was investigated by determining the elemental distribution and HHV's of bio-crudes and are shown in **Table 4**. The change in

catalysts and supports led to varied carbon (69-77 %), oxygen (8-16%), hydrogen (8-10 %) and nitrogen (5-7 %) content of bio-crude. Apart from FeO_x/CeO₂, adding iron-oxide to different supports caused an increase in oxygen content by 2-6 wt% and a decrease in the carbon content by 2-3%. The increase in the heteroatomic contents of bio-crudes produced by supported iron oxides reduced the bio-crude HHV's in comparison to their supports. Catalysts with higher fractions of Fe²⁺ relative to Fe³⁺ (FeO_x/VC, FeO_x/SiO₂-Al₂O₃ and FeO_x/ZSM-5) (Table 3) increased the oxygen content of bio-crudes. Despite the reduction in the HHV's in some cases, the overall energy recoveries that consider the combined factors of bio-crude yields and HHV's improved by 4-9% (Table 4). From the energy recovery perspective FeO_x/SiO₂-Al₂O₃ seems to be the best combination with ER greater than 95 %.

Table 4

Elemental compositions of bio-crudes produced from HTU of food waste at 300 °C, 21 MPa and 1h. (Data presented as mean ± standard deviation, n≥3).

	N (%)	C (%)	H (%)	S (%)	O (%)	HHV (MJ/kg)	ER (%)
No Catalyst	6.50±0.23	70.72±0.42	8.53±0.56	0.21±0.02	14.03±0.74	33.8	87.06
VC	6.61±0.34	73.76±0.37	8.48±0.48	0.22±0.01	10.93±0.69	35.1	82.89
FeO _x /VC	6.12±0.27	68.91±0.49	8.59±0.76	0.20±0.01	16.46±0.94	32.6	86.97
FeO _x MoO _x /VC	7.26±0.44	74.19±0.72	9.28±0.74	0.21±0.01	9.07±1.06	36.4	86.33
CeO ₂	5.80±0.24	71.10±0.32	9.51±0.61	0.23±0.02	12.36±0.73	35.6	85.21
FeO _x /CeO ₂	6.77±0.35	76.64±0.54	8.86±0.65	0.22±0.01	7.50±0.92	36.9	76.70
SiO ₂ -Al ₂ O ₃	5.17±0.27	74.11±0.32	9.92±0.62	0.20±0.02	10.60±0.75	36.9	86.31
FeO _x /SiO ₂ -Al ₂ O ₃	5.77±0.47	72.31±0.68	8.99±0.70	0.21±0.02	12.66±1.08	35.0	95.22
ZSM-5	5.12±0.23	72.30±0.48	8.39±0.55	0.21±0.01	13.81±0.77	34.1	77.13
FeO _x /ZSM-5	5.29±0.34	70.51±0.52	8.12±0.86	0.20±0.02	16.05±1.06	33.0	85.79

3.4 Composition of bio-crudes

The major compounds detected in bio-crude were unsaturated fatty acids, fatty acid amides (FAA), nitrogen heterocyclic compounds (pyrroles, pyrazines, indoles), and oxygen heterocyclic compounds as displayed in Fig. 5a (also see supplementary material for details). A combination of GC-MS data, Van Krevelen chart (see Fig 7), and literature studies were used to elucidate the

influence of various catalysts and supports on reaction pathways. The widely accepted route for the generation of fatty acid is through hydrolysis of triglycerides. The main fatty acid compounds found in this study were octadecanoic, octadecenoic and oleic acids. Fatty acids may further condensate with amines generated from the decomposition of the protein derived amino acids to produce fatty acid amides via amidation [33], [34]. Fatty acid amides may further transform to fatty ketones intermediates and finally hydrocarbons [35]. Amides in this work were mostly detected in form of octadeceneamides in addition to tetra-, hexa-, and octadecanamides. Amidation of fatty acids may also increase the bio-crude yields by transforming water miscible amines into bio-crude miscible compounds (also see Figure 6)[36]. Higher bio-crude yields (**Fig. 4**) were also noted for cases containing high relative content of amines (**Fig. 5a**). Protein derived amine groups may also interact with carbonyl groups generated from the hydrolysis of carbohydrates via Maillard reaction to form nitrogen heterocyclic compounds such as pyridines, pyrazines, pyrroles, indoles and piperidines. Nitrogen heterocyclic compounds are mostly miscible in bio-crude, however, some alcohols and ketones forms of piperdines and pyridines compounds such as pyridinols, pyrrolidinones, piperidones and piperdinones has higher affinity for the water phase [37]. The amines are utilized in two competing reactions between amidation and Maillard reaction during HTL that may favor the formation of either amides or N-heterocyclics [38]. The ratio of amides and N-heterocyclic in **Fig. 5** was between 1.6 and 2.9. It was lower for VC (1.6) and SiO₂-Al₂O₃ (1.8) which may imply higher selectivity toward Maillard reaction. Adding iron-oxide catalyst on all supports except CeO₂ increased the relative ratio of amides which suggest an increased selectivity toward amidation. The higher production of N-heterocyclic compounds using CeO₂ (**Fig 5**) is attributed to the promotion of dehydration and decarboxylation reactions. An increase in cyclic ketones and N-heterocyclic compounds accompanied by a reduction in carboxylic acids were found in FeO_x/CeO₂ bio-crudes which were also found to promote dehydration routes. Ketonization of carboxylic acids via dehydration and decarboxylation routes have been evidenced using CeO₂ based catalysts in other studies [39]. Cyclic ketones such as cyclopentanone are generally produced by dehydration of carboxylic acids [40], or from the hydrogenation of 5-HMF compounds produced during the hydrolysis of carbohydrates [41], [42]. A summary of the reaction pathways is depicted in **Fig. 6**.

As observed in Van Krevelen chart (**Fig. 7**), CeO₂ and SiO₂-Al₂O₃ promoted higher alkylation reactions, possibly via Friedel-Craft alkylation routes induced by hydronium ions [43]. The

reaction trajectory changed into promoting dehydration and decarboxylation reactions after the addition of iron-oxide to CeO_2 , as is also seen by the decrease in the relative content of acids and increase in N-heterocyclics and benzene derivatives (**Fig. 5**). The use of VC promoted dehydration reaction in comparison to the non-catalytic case. The increase in nitrogen content and N-heterocyclic compounds (pyrroles, pyrazines, etc.) of bio-crude while using VC can also be an outcome of dehydration reactions through furans and amino intermediates [44], [45]. The presence of MoO_x in $\text{FeO}_x\text{-MoO}_x/\text{VC}$ promoted alkylation (**Fig. 7** and **Fig. 5b**) and amination (high N/C in **Table 4**) reactions. An increase in relative content of amines and benzene derivatives was observed for $\text{FeO}_x\text{-MoO}_x/\text{VC}$ in comparison to FeO_x/VC (**Fig. 5b**). The increase in amination reactions may also relate to increase in water-soluble and gaseous reactions in **Fig. 4**. The use of $\text{FeO}_x/\text{ZSM-5}$ lead to increased dealkylations reactions, due to the nature of ZSM-5 catalysts (generally used for cracking reactions). Iron-oxide on $\text{SiO}_2\text{-Al}_2\text{O}_3$ support lowered the alkylation reactions while increasing amides (**Fig. 7**). The conversion of acids to amides can be observed from increase in ratio between acids and amides in **Fig. 5a** (from 0.86 to 2.84). The formation of amides from carboxylic acids was least favoured using ZSM-5 and $\text{FeO}_x/\text{ZSM-5}$ with a ratio around 0.9. Amides were lower than the acids unlike bio-crudes from other supports (**Fig. 5a**). The deoxygenation and oxygenation routes were also linked to the chemical state of iron-oxide catalysts, having higher fraction of Fe^0 relative to Fe^{3+} seem to have promoted oxygenation routes as shown from the increase in oxygen content in bio-crudes produced by FeO_x/VC , $\text{FeO}_x/\text{SiO}_2\text{-Al}_2\text{O}_3$ and $\text{FeO}_x/\text{ZSM-5}$. In contrast, having Fe^0 and Mo^0 sites in $\text{FeO}_x/\text{CeO}_2$ and $\text{FeO}_x\text{-MoO}_x/\text{VC}$ promoted deoxygenation routes and produced bio-crudes with lower relative oxygen content in bio-crudes.

$^1\text{H-NMR}$ was used as a complementary technique to study the changes in bio-crude functional groups [46] (also refer to FTIR results in the supplementary material). It is noted that the catalyst promoting dehydration reactions ($\text{FeO}_x/\text{CeO}_2$) were also found to result in the highest aromatics distribution, range 6-8.5 ppm (**Fig. 7** and **Fig. 5b**), which is in-agreement with the increase in benzene derivatives and N-heterocyclics (**Fig. 5a** and **Fig. 6**). Alkanes protons were high in $\text{FeO}_x\text{-MoO}_x/\text{VC}$ bio-crude which may also explain the alkylation route found in **Fig. 7**. The increase in the unsaturated and heteroatomic protons found in the region 1.5-3.0 ppm correlate well with the increase in Fe^{2+} ratios in FeO_x/VC , $\text{FeO}_x/\text{ZSM-5}$ and $\text{FeO}_x/\text{SiO}_2\text{-Al}_2\text{O}_3$ bio-crudes, which may suggest that the possible reason for higher bio-crude yields is the increase in the fractions of fatty

amides and the fatty acids showing lower deoxygenation trajectories in Van Krevelen chart which indicate lower decarboxylation activity for fatty acid conversions (Fig. 7).

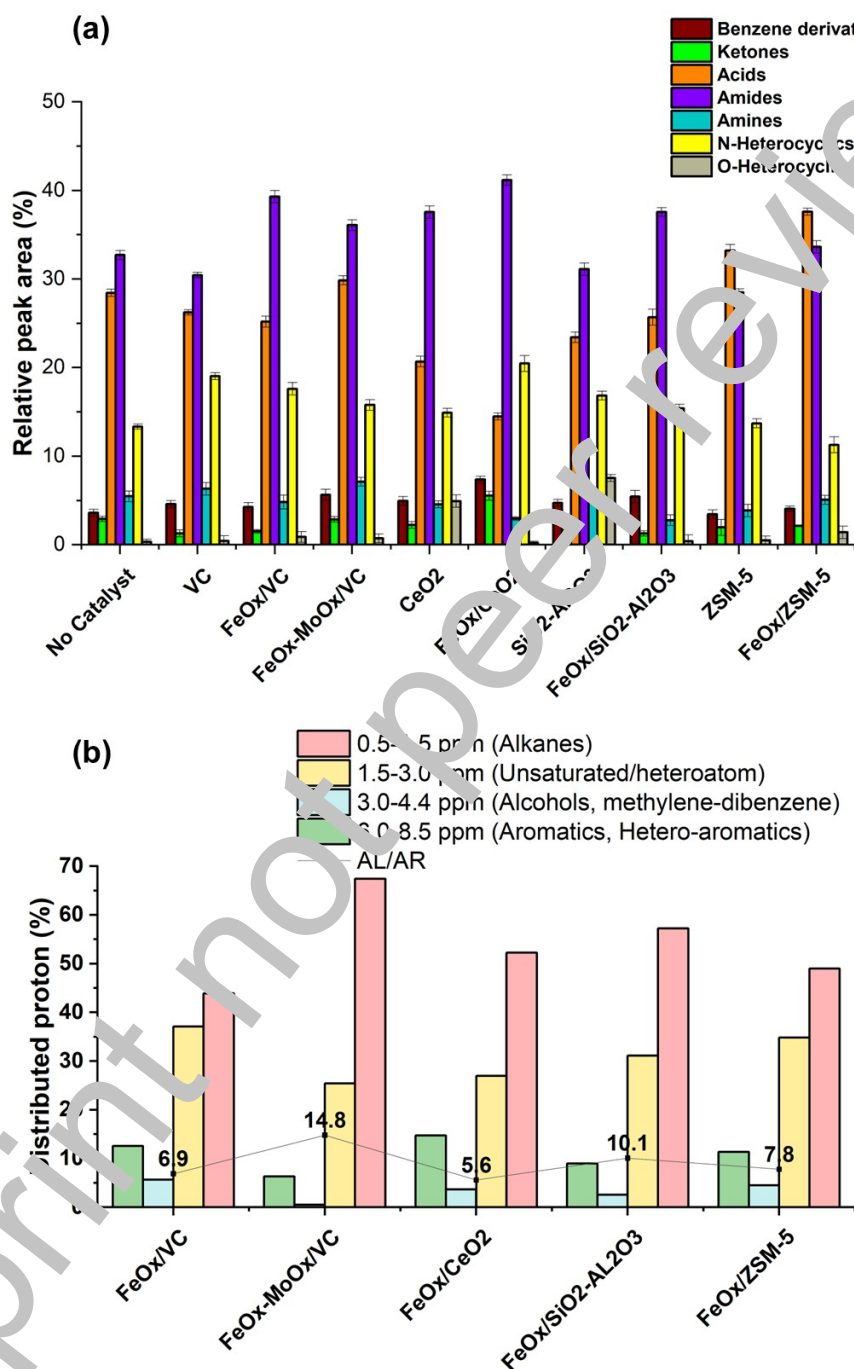


Fig. 5. Chemical compositions of bio-crudes produced by catalytic HTL of food waste at 300 °C, 21 MPa and 1h obtained from a) GC-MS (Replicates with n=2 and error represented as standard deviation) and b) 1H-NMR (AL: aliphatic compounds and AR: aromatics)

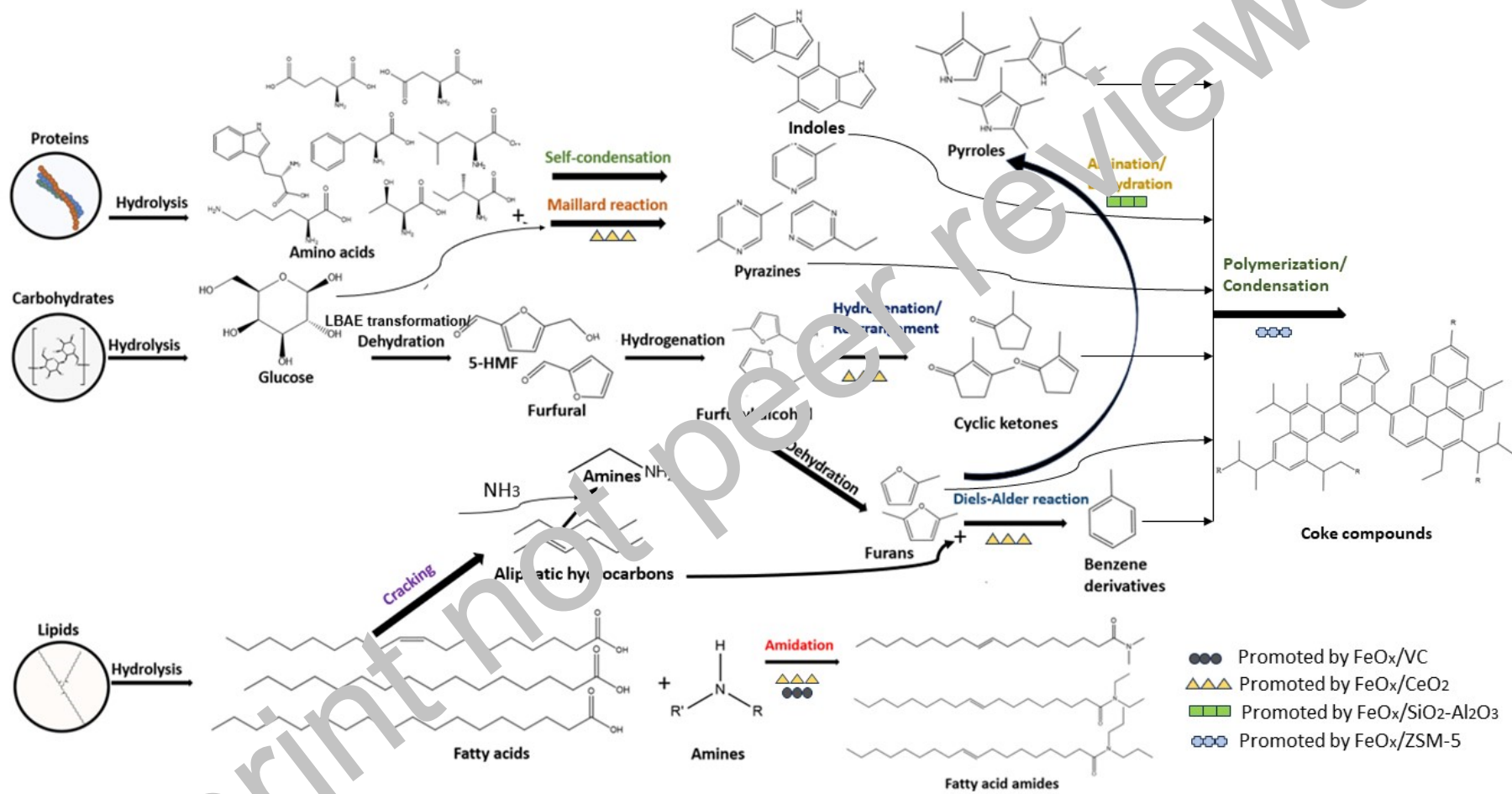


Fig. 6. Proposed reaction pathways for HTL of food waste

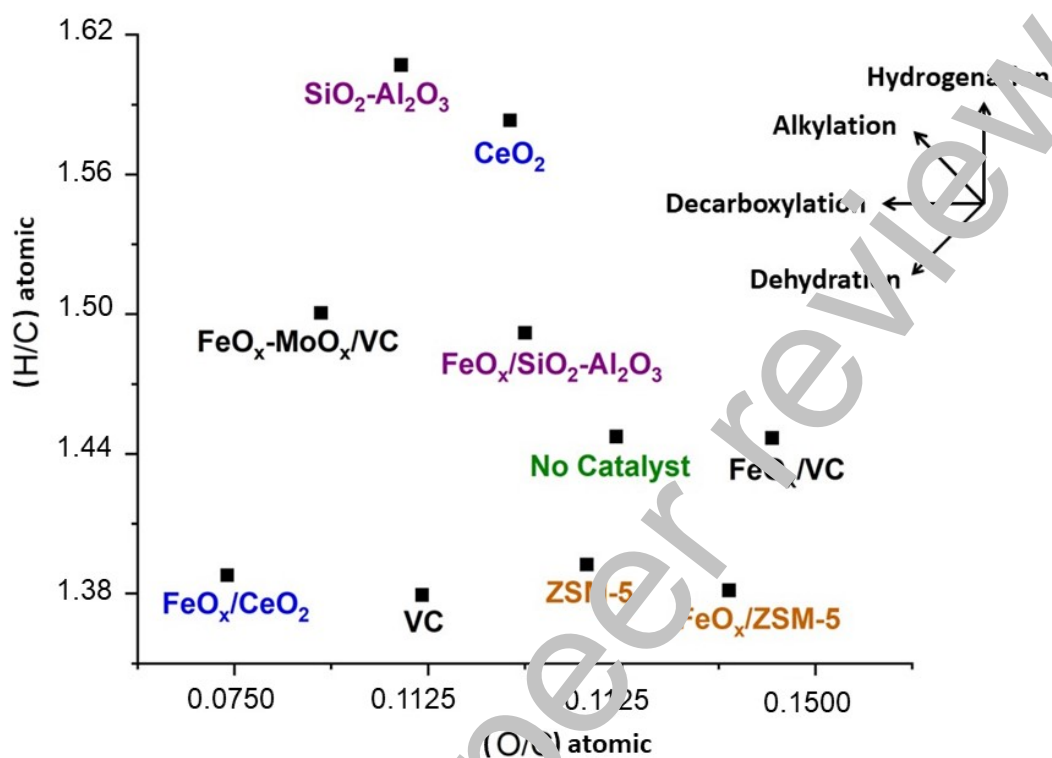


Fig. 7. Van Krevelen chart and trajectories of bio-crudes produced from catalysts with and without iron sites

3.5 Boiling point distribution

The boiling point distribution of bio-crudes classified into following distillation cuts: gasoline (<190 °C), jet fuel (190-290 °C), diesel (290-340 °C) and heavy oil (>340 °C) is shown in **Fig. 8**. Catalysts promoting the formation of N-heterocyclics (e.g. Pyrazine, ethyl-, Pyrazine, 2,5-methyl-, Pyrazine, 2,5-dimethyl-3-propyl-, 1H-Pyrrole, 2,3,4,5-tetramethyl-, Indole) increased the distribution of jet fuel and gasoline range (see **Fig. 5a**). Catalysts that increased the percentage of fatty acids (e.g. Oleic acid and 6-Octadecenoic acid) and fatty amides (e.g. 9-Octadecenamide, (Z)-) in bio-crudes led to the increased distribution of diesel and heavy oil fractions. Supported iron oxide catalysts increased the heavy fractions of bio-crudes in comparison to their supports possibly due to increased activity of condensation reactions and hence asphaltenes (see information about asphaltenes in the supplementary material).

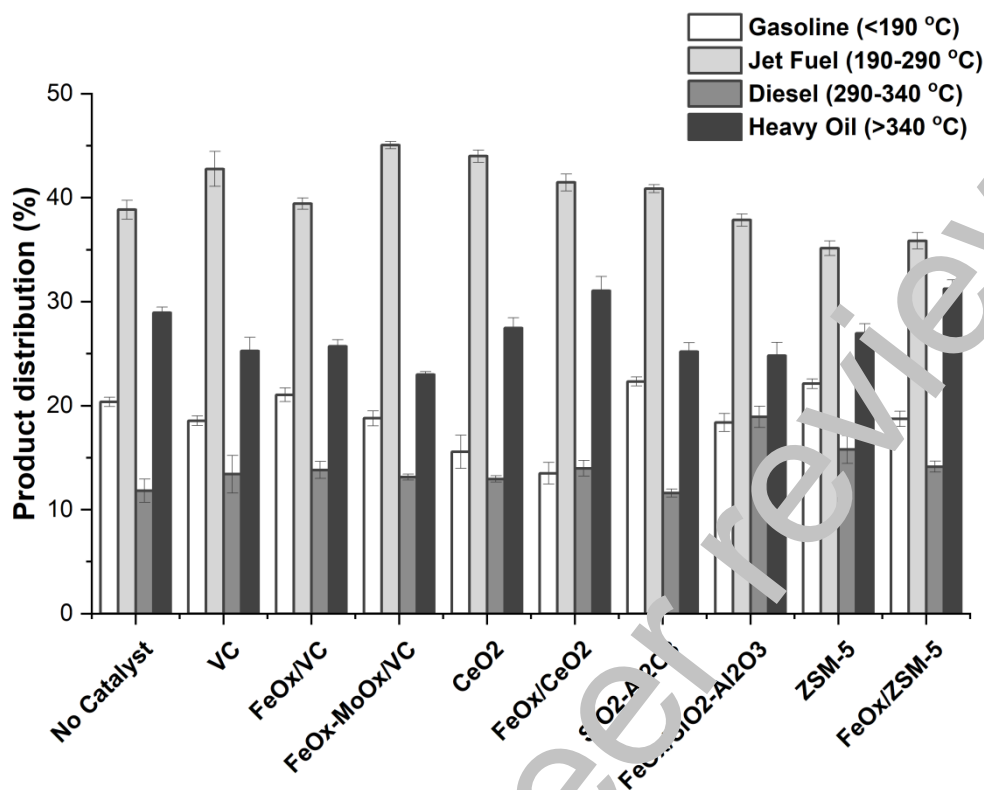


Fig. 8. boiling point distribution of bio-crude classified into different distilled fractions (Replicates with $n \geq 2$ and error represented as standard deviation).

3.5 Catalyst deactivation and reusability

3.5.1 Characterization of spent catalysts

The changes in chemical states of catalysts after reaction were examined by XPS (see **Fig. 9**). Fractions of Fe^{3+} increased relative to Fe^{2+} which indicates that iron was oxidized during HTL processing. The fraction of Fe^{3+} appeared lower in the spent $\text{FeO}_x\text{-MoO}_x\text{/VC}$ catalyst in comparison to the fresh catalyst. The decrease in the Fe^{3+} was associated with the chemical shift of Mo^{5+} to Mo^{4+} , which indicate that Molybdenum was oxidized while iron was reduced during HTL (**Fig. 9**) (also see supporting information). The spent $\text{FeO}_x\text{-MoO}_x\text{/VC}$ also shows the formation of Mo nitrides and MoC sites at binding energies 229.6 eV and 227.7 eV [47], [48]. XPS spectra of spent catalysts also reveal the presence of CaCO_3 sites near 347.5 eV, C-O-P sites near 134.8 eV and Fe-P near 133.8 eV [49]–[51]. The distribution of iron and other elements on spent catalysts is determined by SEM-EDX mapping (**Fig. 10a**) and TEM-EDX (**Fig. 10b**).

Elements found in food waste such as Ca and P were deposited on catalysts and appeared at close proximity to iron which may indicate poisoning effects and potential source of catalyst deactivation.

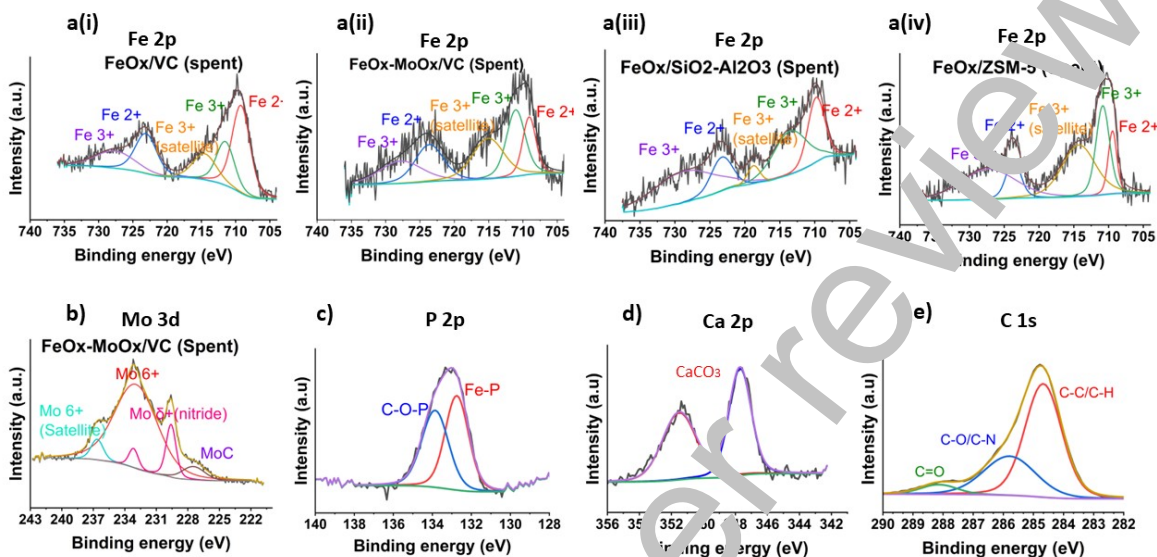


Fig. 9. XPS spectrum of a) Fe 2p and b) Mo 3d c) in spent iron-supported catalysts and c) P 2p d) Ca 2p e) C 1s in spent FeOx/SiO₂-Al₂O₃ catalyst

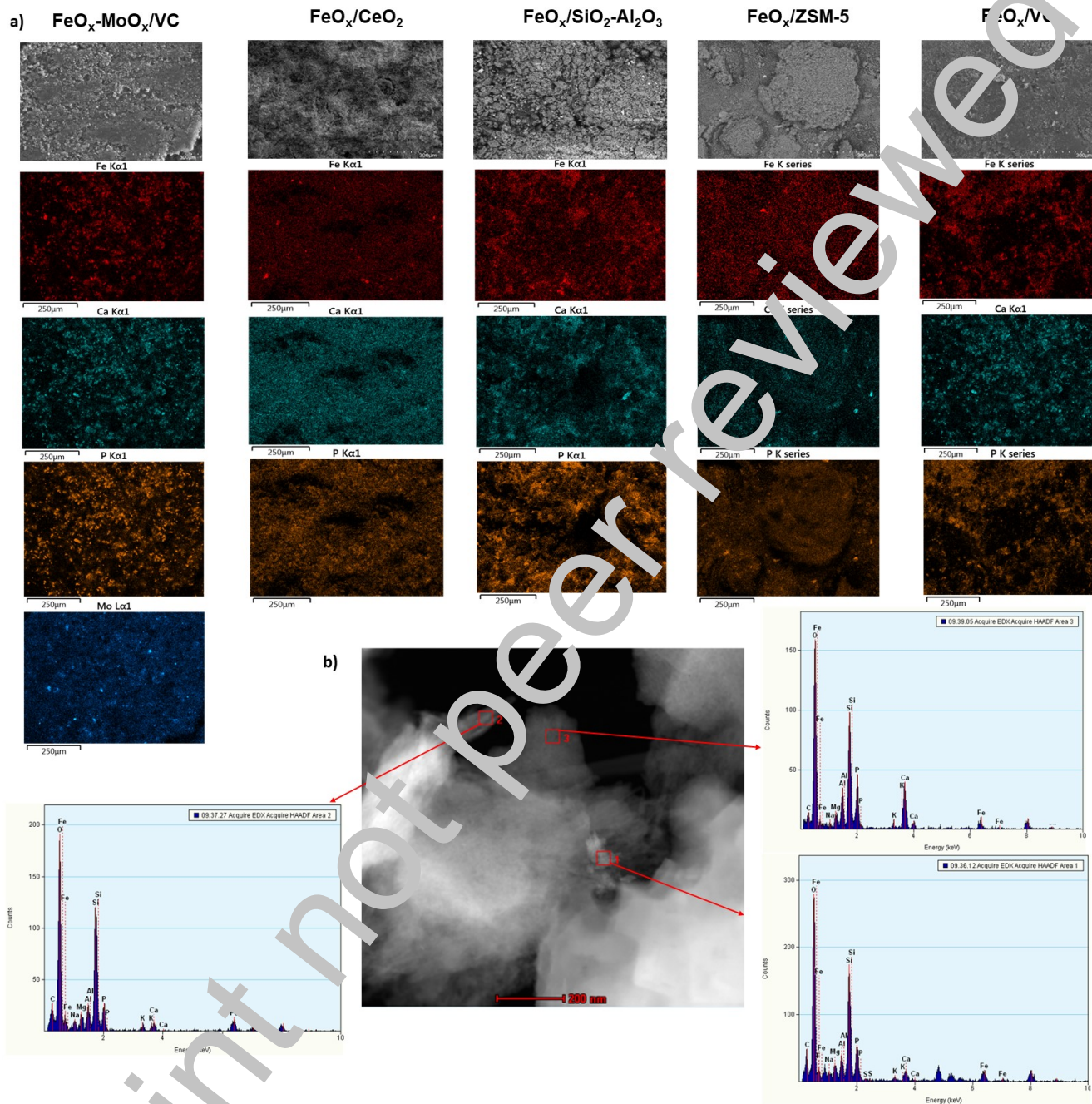


Fig. 10. elemental distributions of spent iron-supported catalyst using a) SEM-EDX mapping and b) TEM-EDX ($\text{FeO}_x/\text{SiO}_2\text{-Al}_2\text{O}_3$ spent catalyst)

Coke deposited on spent catalysts was analysed using TGA experiments. Coke is referred to the carbonaceous deposits on heterogeneous catalysts and typically oxidizes at 450–470 °C for slightly developed coke and 520–530 °C for more condensed coke [52], [53]. The change in iron-oxide

catalyst support influences coke formation as displayed in TG curves in **Fig. 11a**. The main DTG peaks were found at temperatures near 316 °C for spent $\text{FeO}_x/\text{CeO}_2$, 284 °C and 447 °C for spent $\text{FeO}_x/\text{SiO}_2\text{-Al}_2\text{O}_3$, while 344 °C and 423 °C for spent $\text{FeO}_x/\text{ZSM-5}$ (**Fig. 11b**). The amount of coke (weight loss at temperatures higher than 400 °C) was found in the order of $\text{FeO}_x/\text{ZSM-5} > \text{FeO}_x/\text{SiO}_2\text{-Al}_2\text{O}_3 > \text{FeO}_x/\text{CeO}_2$. CeO_2 supported catalysts showed possibly adsorbed organics rather than coke as evidenced by peaks at much lower temperature. The presence of oxygen vacancies have been found to increase the resistance of catalyst sites to formulate high molecular weight fractions in biomass processing [54].

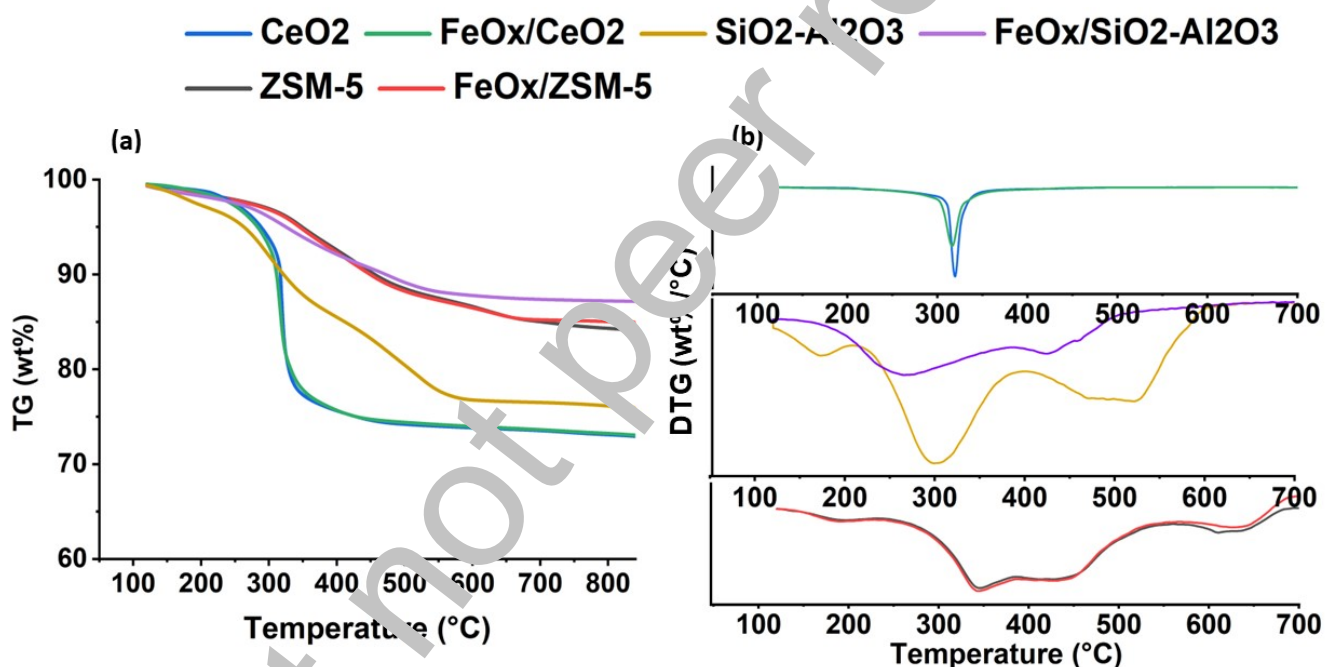


Fig. 11. Analysis of spent catalysts by a) TG thermogram and b) DTG curves

3.5.2 Catalyst reusability

The catalyst with the highest energy recovery was chosen for reusability tests. The catalyst was recycled as is without pre-treatments between HTL tests. The catalyst support $\text{SiO}_2\text{-Al}_2\text{O}_3$ showed reasonable hydrothermal stability with minor indications of dealumination or desilication after three cycles with Si/Al reduction from 5.9 to 5.4. The activity of $\text{FeO}_x/\text{SiO}_2\text{-Al}_2\text{O}_3$ catalyst dropped as seen from the reduction in yields and energy recoveries in **Fig. 12**. The deactivation of recycled

catalysts may be attributed to the decrease in the available active sites and the increase in the P and Ca elements near FeOx (Fig. 12 and Fig. 10). The sintering of active sites can also be another reason for the loss in activity (Fig. 10). The effect of FeOx was lost after the third recycle due to the significant increase in the poisonous elements and the catalyst acted as a support with behaviour closer to that of SiO₂-Al₂O₃ support as displayed in Fig. 12b. It should also be noted that after the third recycle no surface peaks of Fe were observed using XPS analysis.

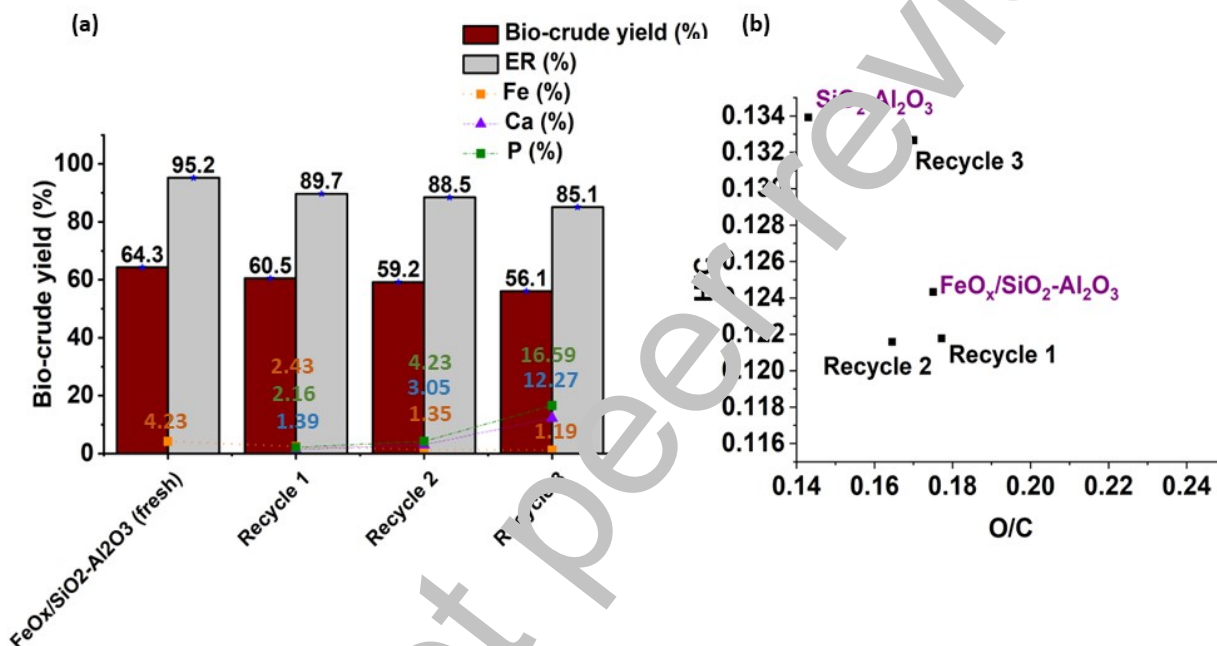


Fig. 12. bio-crude yields, energy recoveries, and metal compositions (ICP-OES) of recycled catalysts, b) Van Krevelen chart of bio-crudes using recycled FeOx/SiO₂-Al₂O₃ catalyst

4 Conclusion

Iron-oxide supported catalysts were studied over Vulcan carbon (VC), CeO₂, SiO₂-Al₂O₃ and ZSM-5 for HTL of food waste at 300 °C. The change in the support and/or addition of a MoO_x sites provided various fractions of Fe(0), Fe²⁺ and Fe³⁺. Catalysts that produced high bio-crude yields were FeO_x/SiO₂-Al₂O₃, FeO_x/ZSM-5 and FeO_x/VC, which were also found to have higher surface fractions of Fe²⁺ in comparison to other catalysts. The increase in bio-crude yields was also found to be associated with the increase in distributions of unsaturated acids and fatty acid amides. Higher distributions of aromatics were found in catalysts featuring dehydration reactions. Also, catalysts

that promoted the formation of N-heterocyclic compounds increased the boiling fractions of bio-crudes in gasoline and jet-fuel range, while catalysts that increased the formation of fatty acids and fatty amides increased the distribution of diesel and heavy fractions. The recycling of FeC₂/SiO₂-Al₂O₃ catalyst showed that the catalyst lost its activity after the 3rd cycle and produced yields and elemental distribution close to that of support SiO₂-Al₂O₃. The sources of catalytic deactivation were attributed to the presence of poisonous compounds (mostly Ca and Fe compounds) that masked the active sites. This study manifests the effect of iron-oxide on various supports in promoting certain reaction pathways that influence the bio-crude yields, its composition, and energy recoveries.

CRedit authorship contribution statement

S.A.E: Conceptualization, Methodology, Investigation, Data curation, Visualization, Writing-original draft, **X.J:** Investigation, Validation **O.K:** Investigation, Validation, **M.C:** Investigation **E.A.B:** Conceptualization, Methodology, Supervision, Writing-review and editing. **D.S:** Conceptualization, Methodology, Supervision, Writing- review and editing, Project administration, Funding acquisition.

Declaration of Competing Interest

The authors declare that they have no known competing financial interests or personal relationships that could have appeared to influence the work reported in this paper.

Acknowledgements

The authors gratefully acknowledge the support provided by National Research Council of Canada (Advanced Clean Energy Program) and Government of Canada (Office of Energy Research and Development). The authors would like to thank Mr. Gilles Robertson and Mr. Weiguo Ma for their support in NMR and GC-MS analysis, respectively. The authors would also like to thank Mr. Deepak K. N. and Mr. Andre Zborowski for their assistance in physisorption analysis, Ms. Judy King for ICP-OES analysis, and Dr. Christopher Panaritis for his guidance in catalyst synthesis.

Appendix A. Supplementary data Supplementary

References

- [1] D. Tong *et al.*, “Committed emissions from existing energy infrastructure jeopardize 1.5 °C climate target,” *Nature*, vol. 572, no. 7769, pp. 373–377, 2019, doi: 10.1038/s41586-019-1364-3.
- [2] P. Van Der Werf and J. A. Gilliland, “A systematic review of food losses and food waste generation in developed countries,” *Proceedings of Institution of Civil Engineers: Waste and Resource Management*, vol. 170, no. 2, pp. 66–77, 2017, doi: 10.1680/jwarm.16.00026.
- [3] T. Makov, A. Shepon, J. Kronos, C. Gupta, and M. Chertow, “Social and environmental analysis of food waste abatement via the peer-to-peer sharing economy,” *Nature Communications*, vol. 11, no. 1, 2020, doi: 10.1038/s41467-020-14899-5.
- [4] G. Perkins, N. Batalha, A. Kumar, T. Bhasakar, and M. Konarova, “Recent advances in liquefaction technologies for production of liquid hydrocarbon fuels from biomass and carbonaceous wastes,” *Renewable and Sustainable Energy Reviews*, vol. 115, no. March, p. 109400, 2019, doi: 10.1016/j.rser.2019.109400.
- [5] S. Nagappan *et al.*, “Catalytic hydrothermal liquefaction of biomass into bio-oils and other value-added products – A review,” *Fuel*, vol. 285, no. August 2020, p. 119053, 2021, doi: 10.1016/j.fuel.2020.119053.
- [6] D. C. Elliott, P. Biller, A. B. Ross, A. J. Schmidt, and S. B. Jones, “Hydrothermal liquefaction of biomass: Developments from batch to continuous process,” *Bioresour Technol*, vol. 178, pp. 147–156, 2015, doi: 10.1016/j.biortech.2014.09.132.
- [7] A. R. Gollakota, N. Kishore, and S. Gu, “A review on hydrothermal liquefaction of biomass,” *Renewable and Sustainable Energy Reviews*, vol. 81, no. May 2017, pp. 1378–1392, 2018, doi: 10.1016/j.rser.2017.05.178.

- [8] A. Dimitriadis and S. Bezergianni, "Hydrothermal liquefaction of various biomass and waste feedstocks for biocrude production: A state of the art review," *Renewable and Sustainable Energy Reviews*, vol. 68, no. September 2016, pp. 113–125, 2017, doi: 10.1016/j.rser.2016.09.120.
- [9] D. Xu, G. Lin, S. Guo, S. Wang, Y. Guo, and Z. Jing, "Catalytic hydrothermal liquefaction of algae and upgrading of biocrude : A critical review," *Renewable and Sustainable Energy Reviews*, vol. 97, no. November 2017, pp. 103–118, 2018, doi: 10.1016/j.rser.2018.08.042.
- [10] H. C. Ong, W. H. Chen, A. Farooq, Y. Y. Gan, K. T. Lee, and V. Ashokkumar, "Catalytic thermochemical conversion of biomass for biofuel production: A comprehensive review," *Renewable and Sustainable Energy Reviews*, vol. 117, no. August 2018, p. 109266, 2019, doi: 10.1016/j.rser.2019.109266.
- [11] K. S. Egorova and V. P. Ananikov, "Which Metals are Green for Catalysis? Comparison of the Toxicities of Ni, Cu, Fe, Pd, Pt, Rh, and Au Salts," *Angewandte Chemie - International Edition*, vol. 55, no. 40, pp. 12150–12162, 2016, doi: 10.1002/anie.201603777.
- [12] I. Bauer and H. J. Knölker, "Iron catalysis in organic synthesis," *Chemical Reviews*, vol. 115, no. 9, pp. 3170–3387, 2015, doi: 10.1021/cr500425u.
- [13] T. Nordgreen, T. Liljeahl, and K. Sjöström, "Metallic iron as a tar breakdown catalyst related to atmospheric, fluidised bed gasification of biomass," *Fuel*, vol. 85, no. 5–6, pp. 689–694, 2006, doi: 10.1016/j.fuel.2005.08.026.
- [14] T. Nordgreen, V. Nemanova, K. Engvall, and K. Sjöström, "Iron-based materials as tar depletion catalysts in biomass gasification: Dependency on oxygen potential," *Fuel*, vol. 95, pp. 71–78, 2012, doi: 10.1016/j.fuel.2011.06.002.
- [15] O. Sengul *et al.*, "Pyrolysis of municipal solid waste with iron-based additives: A study on the kinetic, product distribution and catalytic mechanisms," *Journal of Cleaner Production*, vol. 258, p. 120682, 2020, doi: 10.1016/j.jclepro.2020.120682.

- [16] S. T. Nguyen, T. M. Le, and H. Van Nguyen, "Iron-catalyzed fast hydrothermal liquefaction of *Cladophora socialis* macroalgae into high quality fuel precursor," *Bioresource Technology*, vol. 337, Oct. 2021, doi: 10.1016/j.biortech.2021.125445.
- [17] G. Govindasamy, R. Sharma, and S. Subramanian, "Studies on the effect of heterogeneous catalysts on the hydrothermal liquefaction of sugarcane bagasse to low-oxygen-containing bio-oil," *Biofuels*, vol. 10, no. 5, pp. 665–675, 2019, doi: 10.1080/17597269.2018.1433967.
- [18] L. Tai, B. de Caprariis, M. Scarsella, P. De Filippis, and F. Marra, "Improved Quality Bio-Crude from Hydrothermal Liquefaction of Oak Wood Assisted by Zero-Valent Metals," *Energy and Fuels*, vol. 35, no. 12, pp. 10023–10034, Jun. 2021, doi: 10.1021/acs.energyfuels.1c00889.
- [19] B. de Caprariis, I. Bavasso, M. P. Bracciale, M. Damizia, P. De Filippis, and M. Scarsella, "Enhanced bio-crude yield and quality by reductive hydrothermal liquefaction of oak wood biomass: Effect of iron addition," *Journal of Analytical and Applied Pyrolysis*, vol. 139, no. January, pp. 123–130, 2019, doi: 10.1016/j.jaap.2019.01.017.
- [20] J. S. Saral and P. Ranganathan, "Catalytic hydrothermal liquefaction of *Spirulina platensis* for biocrude production using Red mud," *Biomass Conversion and Biorefinery*, vol. 12, no. 1, pp. 195–208, 2022, doi: 10.1007/s13399-021-01447-4.
- [21] A. Rojas-Pérez *et al.*, "Catalytic effect of ultrananocrystalline Fe₃O₄ on algal bio-crude production via HTL process," *Nanoscale*, vol. 7, no. 42, pp. 17664–17671, 2015, doi: 10.1039/c5nr04407a.
- [22] W. Wang, Y. Xu, X. Wang, B. Zhang, W. Tian, and J. Zhang, "Hydrothermal liquefaction of microalgae over transition metal supported TiO₂ catalyst," *Bioresource Technology*, vol. 250, no. November 2017, pp. 474–480, 2018, doi: 10.1016/j.biortech.2017.11.051.
- [23] T. F. Robin, A. B. Ross, A. R. Lea-Langton, and J. M. Jones, "Stability and activity of copper doped transition metal zeolites in the hydrothermal processing," *Frontiers in Energy Research*, vol. 3, no. DEC, 2015, doi: 10.3389/fenrg.2015.00051.

- [24] K. Parizeau, M. von Massow, and R. C. Martin, "Directly observing household food waste generation using composition audits in a Canadian municipality," *Waste Management*, vol. 135, no. May, pp. 229–233, 2021, doi: 10.1016/j.wasman.2021.08.039.
- [25] A. Bernstad Saraiva Schott and A. Cánovas, "Current practice, challenges and potential methodological improvements in environmental evaluations of food waste prevention - A discussion paper," *Resources, Conservation and Recycling*, vol. 101, pp. 132–142, 2015, doi: 10.1016/j.resconrec.2015.05.004.
- [26] N. Carroll *et al.*, "Association between diet quality and food waste in Canadian families: A cross-sectional study," *Nutrition Journal*, vol. 19, no. 1, pp. 1–8, 2020, doi: 10.1186/s12937-020-00571-7.
- [27] S. A. Ebrahim, G. Robertson, X. Jiang, E. A. Baranova, and D. Singh, "Catalytic hydrothermal liquefaction of food waste: Influence of catalysts on bio-crude yield, asphaltenes, and pentane soluble fractions," *Fuel*, vol. 324, no. PA, p. 124452, 2022, doi: 10.1016/j.fuel.2022.124452.
- [28] G. Robertson, K. V. Adiningtyas, S. A. Ebrahim, L. Scoles, E. A. Baranova, and D. Singh, "Understanding the nature of bio-asphaltenes produced during hydrothermal liquefaction," *Renewable Energy*, vol. 173, pp. 128–140, 2021, doi: 10.1016/j.renene.2021.03.099.
- [29] C. Panaritis, J. Zgheib, S. A. H. Forahim, M. Couillard, and E. A. Baranova, "Electrochemical in-situ activation of Fe-oxide nanowires for the reverse water gas shift reaction," *Applied Catalysis B: Environmental*, vol. 269, no. October 2019, p. 118826, 2020, doi: 10.1016/j.apcatb.2020.118826.
- [30] R. Wu, J. Beutler, C. Price, and L. L. Baxter, "Biomass char particle surface area and porosity dynamics during gasification," *Fuel*, vol. 264, no. October 2019, p. 116833, 2020, doi: 10.1016/j.fuel.2019.116833.
- [31] D. D. Jana, T. Boningari, and P. G. Smirniotis, "High-temperature water-gas shift over Fe-Ce/Co spinel catalysts : Study of the promotional effect of Ce and Co," *Molecular Catalysis*, vol. 451, pp. 20–32, 2018, doi: 10.1016/j.mcat.2017.10.013.

- [32] J. Baltrusaitis *et al.*, “Generalized molybdenum oxide surface chemical state XPS determination via informed amorphous sample model,” *Applied Surface Science*, vol. 226, pp. 151–161, 2015, doi: 10.1016/j.apsusc.2014.11.077.
- [33] R. M. Lanigan and T. D. Sheppard, “Recent developments in amide synthesis: Direct amidation of carboxylic acids and transamidation reactions,” *European Journal of Organic Chemistry*, no. 33, pp. 7453–7465, 2013, doi: 10.1002/ejoc.201300573.
- [34] S. Chiaberge *et al.*, “Amides in Bio-oil by Hydrothermal Liquefaction of Organic Wastes: A Mass Spectrometric Study of the Thermochemical Reaction Products of Binary Mixtures of Amino Acids and Fatty Acids,” *Energy & Fuels*, vol. 27, no. 9, pp. 5287–5297, Sep. 2013, doi: 10.1021/ef4009983.
- [35] M. Watanabe, T. Iida, and H. Inomata, “Decomposition of a long chain saturated fatty acid with some additives in hot compressed water,” vol. 47, pp. 3344–3350, 2006, doi: 10.1016/j.enconman.2006.01.009.
- [36] F. Cheng *et al.*, “Hydrothermal liquefaction of high- and low-lipid algae: Bio-crude oil chemistry,” *Applied Energy*, vol. 206, no. May, pp. 278–292, 2017, doi: 10.1016/j.apenergy.2017.08.105.
- [37] G. Chen *et al.*, “Effects of reaction conditions on products and elements distribution via hydrothermal liquefaction of duckweed for wastewater treatment,” *Bioresource Technology*, vol. 317, no. June, p. 124033, Dec. 2020, doi: 10.1016/j.biortech.2020.124033.
- [38] Y. Fan, U. Heilmann, M. Raffelt, and N. Dahmen, “The influence of lipids on the fate of nitrogen during hydrothermal liquefaction of protein-containing biomass,” *Journal of Analytical and Applied Pyrolysis*, vol. 147, no. October 2019, p. 104798, 2020, doi: 10.1016/j.jap.2020.104798.
- [39] O. Nagashima, S. Sato, R. Takahashi, and T. Sodesawa, “Ketonization of carboxylic acids over CeO₂-based composite oxides,” *Journal of Molecular Catalysis A: Chemical*, vol. 227, no. 1–2, pp. 231–239, Mar. 2005, doi: 10.1016/j.molcata.2004.10.042.

- [40] M. Renz, "Ketonization of carboxylic acids by decarboxylation: Mechanism and scope," *European Journal of Organic Chemistry*, no. 6, pp. 979–988, 2005, doi: 10.1002/ejoc.200400546.
- [41] A. Mittal, H. M. Pilath, and D. K. Johnson, "Direct Conversion of Biomass Carbohydrates to Platform Chemicals: 5-Hydroxymethylfurfural (HMF) and Furfural," *Energy and Fuels*, vol. 34, no. 3, pp. 3284–3293, 2020, doi: 10.1021/acs.energyfuels.9b04147.
- [42] B. Wozniak, A. Spannenberg, Y. Li, S. Hinze, and J. G. de Vries, "Cyclopentanone Derivatives from 5-Hydroxymethylfurfural via 1-Hydroxyhexane-2,5-dione as Intermediate," *ChemSusChem*, vol. 11, no. 2, pp. 356–359, 2018, doi: 10.1002/cssc.201702100.
- [43] S. Kang, X. Li, J. Fan, and J. Chang, "Classified separation of lignin hydrothermal liquefied products," *Industrial and Engineering Chemistry Research*, vol. 50, no. 19, pp. 11288–11296, 2011, doi: 10.1021/ie2011356.
- [44] Q. Yao, L. Xu, C. Guo, Z. Yuan, Y. Zhang, and Y. Fu, "Selective production of pyrroles via catalytic fast pyrolysis of cellulose under ammonia atmosphere at low temperature," *Journal of Analytical and Applied Pyrolysis*, vol. 124, pp. 409–414, 2017, doi: 10.1016/j.jaap.2017.03.004.
- [45] K. M. Klinger, F. Liebner, A. Fritz, A. Potthast, and T. Rosenau, "Formation and ecotoxicity of N-heterocyclic compounds on ammoxidation of mono- and polysaccharides," *Journal of Agricultural and Food Chemistry*, vol. 61, no. 38, pp. 9004–9014, 2013, doi: 10.1021/jf4019596.
- [46] D. R. Vardon *et al.*, "Chemical properties of biocrude oil from the hydrothermal liquefaction of *Spirulina* algae, swine manure, and digested anaerobic sludge," *Bioresource Technology*, vol. 102, no. 17, pp. 8295–8303, 2011, doi: 10.1016/j.biortech.2011.06.041.
- [47] A. Foy, A. Serov, K. Artyushkova, E. L. Brosha, P. Atanassov, and T. L. Ward, "Facile synthesis of high surface area molybdenum nitride and carbide," *Journal of Solid State Chemistry*, vol. 228, pp. 232–238, 2015, doi: 10.1016/j.jssc.2015.05.007.

- [48] H. Wu and K. Lian, "The Development of Pseudocapacitive Molybdenum Oxynitride Electrodes for Supercapacitors," *ECS Transactions*, vol. 58, no. 25, pp. 67–75, 2014, doi: 10.1149/05825.0067ecst.
- [49] M. L. Granados *et al.*, "Biodiesel from sunflower oil by using activated calcium oxide," *Applied Catalysis B: Environmental*, vol. 73, no. 3–4, pp. 317–326, May 2007, doi: 10.1016/j.apcatb.2006.12.017.
- [50] W. Li *et al.*, "Insights into the promotion role of phosphorus doping on carbon as a metal-free catalyst for low-temperature selective catalytic reduction of NO with NH₃," *RSC Advances*, vol. 10, no. 22, pp. 12908–12919, 2020, doi: 10.1039/D0RA01654C.
- [51] J. Liu, Y. Zhu, F. Du, and L. Jiang, "Iron/Nitrogen/Phosphorus Co-Doped Three-Dimensional Porous Carbon as a Highly Efficient Electrocatalyst for Oxygen Reduction Reaction," *Journal of The Electrochemical Society*, vol. 166, no. 13, pp. F935–F941, Aug. 2019, doi: 10.1149/2.1081912jes.
- [52] S. Du, J. A. Valla, and G. M. Bollas, "Characteristics and origin of char and coke from fast and slow, catalytic and thermal pyrolysis of biomass and relevant model compounds," *Green Chemistry*, vol. 15, no. 11, p. 3214, 2013, doi: 10.1039/c3gc41581c.
- [53] G. Elordi, M. Olazar, G. Lopez, P. Castaño, and J. Bilbao, "Role of pore structure in the deactivation of zeolites (HZSM-5, H β and HY) by coke in the pyrolysis of polyethylene in a conical spouted bed reactor," *Appl Catal B*, vol. 102, no. 1–2, pp. 224–231, Feb. 2011, doi: 10.1016/j.apcatb.2010.12.002.
- [54] L. T. Do *et al.*, "Catalytic hydrocracking of pyrolytic lignin in supercritical methanol over nickel-niobium/ceria-deposited HZSM-5," *Fuel Processing Technology*, vol. 250, no. June, p. 107878, Nov. 2023, doi: 10.1016/j.fuproc.2023.107878.